

ARTICLE

Received 1 Aug 2011 | Accepted 7 Mar 2012 | Published 10 Apr 2012

DOI: 10.1038/ncomms1777

Nanodomain Ca^{2+} of Ca^{2+} channels detected by a tethered genetically encoded Ca^{2+} sensor

Lai Hock Tay¹, Ivy E. Dick¹, Wanjun Yang¹, Marco Mank³, Oliver Griesbeck³ & David T. Yue^{1,2}

Coupling of excitation to secretion, contraction and transcription often relies on Ca^{2+} computations within the nanodomain—a conceptual region extending tens of nanometers from the cytoplasmic mouth of Ca^{2+} channels. Theory predicts that nanodomain Ca^{2+} signals differ vastly from the slow submicromolar signals routinely observed in bulk cytoplasm. However, direct visualization of nanodomain Ca^{2+} far exceeds optical resolution of spatially distributed Ca^{2+} indicators. Here we couple an optical, genetically encoded Ca^{2+} indicator (TN-XL) to the carboxy tail of $\text{Ca}_v2.2$ Ca^{2+} channels, enabling near-field imaging of the nanodomain. Under total internal reflection fluorescence microscopy, we detect Ca^{2+} responses indicative of large-amplitude pulses. Single-channel electrophysiology reveals a corresponding Ca^{2+} influx of only 0.085 pA, and fluorescence resonance energy transfer measurements estimate TN-XL distance to the cytoplasmic mouth at ~55 Å. Altogether, these findings raise the possibility that Ca^{2+} exits the channel through the analogue of molecular portals, mirroring the crystallographic images of side windows in voltage-gated K channels.

¹ Department of Biomedical Engineering, Calcium Signals Laboratory, Ross Building, Room 713, 720 Rutland Avenue, Baltimore, Maryland 21205-2196, USA. ² Department of Neuroscience, Johns Hopkins University School of Medicine, Ross Building, Room 713, 720 Rutland Avenue, Baltimore, Maryland 21205-2196, USA. ³ AG Zelluläre Dynamik, Max-Planck-Institut für Neurobiologie, Am Klopferspitz 18, 82152 Martinsried, Germany. Correspondence and requests for materials should be addressed to D.T.Y. (email: dyue@jhmi.edu).

Ca²⁺ signals extend pervasively across the intracellular expanse of most cells; yet, these signals exhibit remarkable specificity in activating appropriate Ca²⁺-modulated targets. Understanding how this selectivity arises remains a foremost question in Ca²⁺ biology^{1,2}. One strategy is to co-localize at molecular dimensions Ca²⁺ sources and targets. This co-localization is crucial to the local signalling of Ca²⁺ channels to nearby Ca²⁺-regulated ion channels and enzymes^{3–5} to neurotransmitter release⁶, as well as to excitation–contraction⁷ and excitation–transcription coupling^{8,9}. Intriguingly, co-localized sensors do not always respond preferentially to local Ca²⁺ sources, but can require the far weaker input of remote Ca²⁺ sources acting through a global Ca²⁺ selectivity paradigm¹⁰. Critical to signalling near Ca²⁺ sources is the nature of Ca²⁺ signals within a few tens of nanometers of a Ca²⁺ channel (nanodomain¹¹). Theoretical calculations^{12–16} postulate that nanodomain signals comprise Ca²⁺ pulses of equal and enormous amplitude (~100 μ M), with each pulse synchronized to the millisecond stochastic openings of channels^{10,12}. Beyond the nanodomain, [Ca²⁺] rapidly dissipates with diffusion. Of note, predicted nanodomain [Ca²⁺] amplitudes vary considerably with assumed parameters¹⁷, and elegant experimental estimates of local Ca²⁺ signals^{18,19} only indirectly probe the nanodomain itself. Thus, the critical magnitude of nanodomain Ca²⁺ pulses (Ca_{spike}) has eluded explicit empirical comment. This uncertainty bears on key issues, including how spatial Ca²⁺ decoding occurs within the nanodomain^{10,20–22} and the Ca²⁺ channel number needed to trigger neurotransmitter vesicles^{23–25}.

Why have nanodomain Ca²⁺ signals remained elusive? Although fluorescent Ca²⁺-sensitive chemical dyes have revealed much²⁶, visualization of nanodomain signals via freely diffusible dye molecules far exceeds the resolution limit of far-field microscopic approaches²⁷. In this regime, fluorescence from dye molecules outside the nanodomain will overshadow that from within²⁸. Even when imaged with total internal reflection fluorescence (TIRF) microscopy^{29–31} that illuminates a restricted TIRF volume within ~150 nm of the glass/cell membrane interface, freely diffusible dyes will still report Ca²⁺ from a region several-fold larger than a Ca²⁺ channel³².

One approach is to affix a Ca²⁺ indicator within the nanodomain, so as to support a form of near-field imaging³³. The Ca²⁺-sensitive luminescent protein aequorin represents a traditional candidate³⁴. Recombinant aequorins have long been targeted to various subcellular compartments by genetic means^{35–37} but the limited-amplitude and consumptive nature of aequorin would challenge deployment in a channel nanodomain³⁴. Recently, promising results have been obtained using a biarsenical chemical fluorescent Ca²⁺ indicator (Calcium green FAsH, CaGF) targeted to a tetracycline tag implanted on Ca_v1.2 Ca²⁺ channels³⁸. CaGF features Ca²⁺ affinity and kinetics (K_d , ~55 μ M; off rate, 2 ms^{–1}) well matched to the purported amplitudes and lifetimes of nanodomain Ca²⁺ pulses. Indeed, CaGF was potentially responsive to nanodomain Ca²⁺ fluctuations, but the observed fluorescence signals were highly heterogeneous, to an extent that precluded quantitative Ca²⁺ estimation. This heterogeneity was attributable to the diminutive and variable open probability of Ca_v1.2 channels (~0.1–0.3%), despite constitutive pharmacological manipulation by a channel opener. Indeed, the possibility of a large fraction of electrically silent Ca_v1.2 channels fits with their unusually large ratio of gating charge to ionic current³⁹. Also, although careful controls were performed for nonspecific labelling of other cysteine-rich sites in the cell by CaGF, such indiscriminate attachment would remain a generic concern for approaches involving chemical targeting of sensors. A third approach would be to employ genetically encoded Ca²⁺ indicators (GECIs) as near-field sensors. GECIs allow genetic fusion of sensor to a Ca²⁺ source, offering the greatest potential selectivity in positioning sensors. Among the most popular GECIs

are CFP/YFP-FRET (fluorescence resonance energy transfer)-based molecules such as cameleons⁴⁰, and GFP-intensity-based sensors like GCaMPs⁴¹. All these employ calmodulin (CaM) as their Ca²⁺ sensor, and convert binding of the sensor's own Ca²⁺/CaM with a target peptide into altered optical readouts. When targeted to plasmalemma, cameleons often lose Ca²⁺ sensitivity⁴², potentially via target peptide binding to elevated plasmalemmal CaM⁴³.

Accordingly, we here explore near-field imaging of nanodomain Ca²⁺ using TN-XL, a GECI⁴⁴ based on the Ca²⁺ sensor troponin C. TN-XL exploits Ca²⁺-driven conformational changes without a target peptide, thereby naturally resisting endogenous CaM interference⁴². Our specific approach is to fuse TN-XL to the carboxy terminus of the principle subunit of Ca_v2.2 Ca²⁺ channels, chosen for high open probability⁴⁵, relative absence of silent channels⁴⁶, and abundant plasmalemmal expression⁴⁷. To further improve the TN-XL signal-to-noise ratio at the surface membrane, we utilize TIRF microscopy to selectively illuminate only those Ca_v2.2/TN-XL channels near the surface, thereby attenuating background signal from imperfectly targeted intracellular channels. Finally, to account for the high Ca²⁺ affinity and slow kinetics of GECIs⁴⁴ (off times, 100–900 ms for TN-XL) in the face of millisecond nanodomain Ca²⁺ pulses, we quantify the kinetics of TN-XL readouts, which our previous work suggests can distinguish between differing Ca_{spike} amplitudes⁴⁸. These strategies allow us to resolve nanodomain Ca²⁺ activity of Ca_v2.2 channels undergoing native gating, without pharmacological manipulation.

Results

Functional Ca_v2.2/TN-XL fusions at the surface membrane.

Our strategy for probing nanodomain Ca²⁺ signals (Fig. 1) requires maintained Ca²⁺ responsiveness of genetically encoded sensors situated at the plasmalemma, which is a foremost challenge. Accordingly, we examined whether troponin-based TN-XL could respond to Ca²⁺ when targeted to this environment. As a baseline, Fig. 2a displays the properties of the well-studied, cytoplasmic form of TN-XL⁴⁴. Confocal images of an exemplar HEK293 cell, acquired under CFP and FRET imaging modes, reveal the expected pan-cytoplasmic distribution. An epifluorescence CFP image of another cell also demonstrates this generalized expression, and switching to TIRF mode indicates no preferential TN-XL accumulation within the plasmalemmal footprint of this same cell. To gauge TN-XL responsiveness, we measured, under TIRF imaging, the single-cell CFP (S_C , respective excitation and emission wavelengths at 442 and 485 nm) and FRET fluorescence signals (S_F , excitation and emission at 442 and 545 nm), where the ratio of these signals ($R_{F/C} = S_F/S_C$) furnishes the customary sensor readout of Ca²⁺ (Fig. 2b). In particular, the ratio $R_{F/C}$ was first determined in resting cells with cytoplasmic Ca²⁺ concentration ($\leq 0.1 \mu$ M) well below the K_d of the TN-XL²⁴, thus yielding R_{min} . To subsequently determine R_{max} , Ca_v2.2 channels were co-expressed as conduits of Ca²⁺ entry under whole-cell voltage clamp. To facilitate elevation of intracellular Ca²⁺, minimal internal Ca²⁺ buffering (1 mM EGTA) with elevated 10 mM extracellular Ca²⁺ was employed, such that repetitive step depolarizations (30 mV×500 ms pulses every 15 s) readily saturated $R_{F/C}$ at R_{max} . Thus, the ratio of R_{max} and R_{min} reports sensor dynamic range.

By contrast, for TN-XL fused to the farnesylation motif of Ras (TN-XL-Ras), sensors are sharply localized to the surface membrane in confocal and epifluorescence images (Fig. 2c), and there is marked enrichment within the TIRF footprint. Importantly, the Ca²⁺ dynamic range of TN-XL-Ras is nearly identical (Fig. 2d), despite residence within the plasmalemmal context. Yet more relevant are results for the Ca_v2.2/TN-XL fusions (Fig. 2e). Here constructs appear only partially localized to the surface membrane, consistent with typically imperfect trafficking of recombinant Ca²⁺ channels to plasmalemma⁴⁹. Still, there is substantial focalization

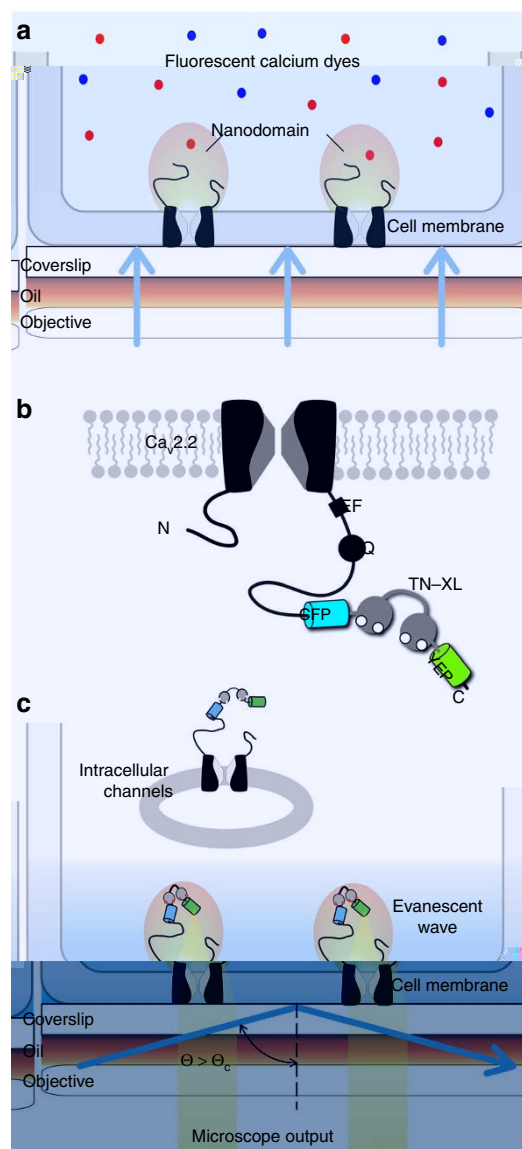


Figure 1 | Approach to resolving channel nanodomain Ca^{2+} signals.

(a) Conventional wide-field imaging using cytosolic chemical fluorescent dyes cannot resolve channel nanodomain Ca^{2+} signals. Blue shading denotes region of fluorescence excitation, which extends throughout the cell under wide-field imaging. (b) Design of the genetically encoded Ca^{2+} indicator TN-XL fused to the carboxy tail of the α_{1B} subunit of a $\text{Ca}_v2.2$ channel, yielding $\text{Ca}_v2.2/\text{TN-XL}$. For orientation, structure-function elements involved in calmodulin regulation are denoted on carboxy terminus²¹: EF, EF-hand region; IQ, IQ-domain for apoCaM binding. CFP denotes enhanced CFP. YFP denotes circularly permuted citrine. (c), $\text{Ca}_v2.2/\text{TN-XL}$ constructs act as a 'near-field' sensor of nanodomain Ca^{2+} . TIRF imaging evanescent wave illuminates only $\text{Ca}_v2.2/\text{TN-XL}$ channels within ~ 150 nm from the glass/cell membrane interface, as indicated by the blue-shaded region. This mode of excitation potentially excludes intracellular channels from consideration. When laser illumination angle Θ exceeds a critical angle Θ_c , TIRF illumination occurs.

of $\text{Ca}_v2.2/\text{TN-XL}$ in the TIRF footprint, suggesting sufficient trafficking for nanodomain experiments (Fig. 1c). Critically, sensor dynamic range is spared when juxtaposed near $\text{Ca}_v2.2$ channels (Fig. 2f).

A second concern is the preservation of $\text{Ca}_v2.2$ channel function upon fusion to TN-XL. Reassuringly, Ca^{2+} currents appeared

nearly identical in $\text{Ca}_v2.2/\text{TN-XL}$ (Fig. 3a, black) and $\text{Ca}_v2.2$ (grey) channels. In fact, fusing TN-XL to $\text{Ca}_v2.2$ enhances opening, as seen from hyperpolarization of tail-activation curves determined with 10-mM extracellular Ca^{2+} as charge carrier (Fig. 3b). Even at the single-channel level, $\text{Ca}_v2.2/\text{TN-XL}$ fusions exhibited robust electrophysiological function, as illustrated by the exemplar single-channel current trace shown at high-gain magnification (Fig. 3c, noisy trace). We used 90 mM Ba^{2+} as a charge carrier to enhance resolution of elementary events, and evoked currents via ramp depolarization to readily resolve the open-channel conduction profile (downwardly convex grey relation). Multiple single-channel sweeps (Fig. 3d), displayed at lower-gain magnification, confirm the overall reproducibility and excellent resolution of elementary events under this protocol. Accordingly, numerous sweeps from multiple patches specify a highly reliable ensemble average current (Fig. 3c, red curve), closely similar to that of $\text{Ca}_v2.2$ channels without sensor fusion⁴⁵. Taking the ratio of the ensemble average current with the open-channel conduction profile (Fig. 3c, red and convex grey curves) yields a plot of open probability P_O versus voltage V (Fig. 3e, gray relation). This plot matches impressively with whole-cell activation (reproduced as open circles), after shifting along the voltage axis to account for contrasting surface-charge effects of single-channel versus whole-cell solutions. As with studies of $\text{Ca}_v2.2$ (ref. 45), the $\text{Ca}_v2.2/\text{TN-XL}$ fusion exhibits a substantial P_O of 0.69 at 30 mV (Fig. 3e, red arrows), a feature advantageous for probing nanodomain Ca^{2+} .

A final prerequisite is that $\text{Ca}_v2.2/\text{TN-XL}$ fusions resist proteolysis. Accordingly, we utilized anti-GFP antibody to perform western immunoblots from cells expressing this construct (Fig. 3f, left lane). The other lanes correspond to cells expressing TN-XL-Ras (~ 71 kD), as well as untransfected cells (no signal). The absence of signal beneath the full-length ~ 320 kD band (Fig. 3f, left lane) substantiates maintained TN-XL fusion to channels (Fig. 3g).

Calibration of TN-XL fused to $\text{Ca}_v2.2$ channels. We next addressed more precise sensor calibration, to facilitate quantitative inferences about nanodomain Ca^{2+} . Both kinetic and steady-state characterization would be ideal, given the millisecond kinetics of Ca^{2+} pulses within channel nanodomains, coupled with the comparatively slow response of free TN-XL (off rates of 1/150 to 1/850 1/ms⁴⁴). Accordingly, we devised a state-mechanism approximation of sensor performance, a 'forward transform' that maps rapid Ca^{2+} transient inputs onto slower sensor outputs, as previously established for an older variant of TN-XL (TN-L15), freely expressed in myocytes⁴⁸. Here we pursued an analogous approach, but attuned to $\text{Ca}_v2.2/\text{TN-XL}$ constructs resident within the TIRF volume and driven by high-amplitude dynamic Ca^{2+} inputs pertinent to channel nanodomains. To produce such inputs, we activated ultra-large $\text{Ca}_v2.2$ Ca^{2+} currents (Fig. 4a) in HEK293 cells, featuring minimal exogenous intracellular Ca^{2+} buffering (1 mM EGTA); this configuration intentionally produced enormous spatial gradients of intracellular Ca^{2+} (Fig. 4b, inset), far exceeding that usually encountered. To estimate these gradients, we simultaneously monitored aggregate Ca^{2+} concentration (Fig. 4b, noisy dark trace), as deduced by imaging the entire cell for signals emanating from 10 μM of the rapid chemical fluorescent Ca^{2+} indicator Fluo 4FF. The measured Ca^{2+} influx (Fig. 4a) and aggregate $[\text{Ca}^{2+}]$ signals were then used to explicitly constrain a radially symmetric Ca^{2+} diffusion mechanism, whose estimates of Ca^{2+} concentration, in differing cellular regions, are shown as red traces in Fig. 4b (Supplementary Fig. S1; Supplementary Methods). The estimated aggregate $[\text{Ca}^{2+}]$ concentration (Fig. 4b, lower red trace) closely approximates its measured analogue (dark noisy trace), and the estimated $[\text{Ca}^{2+}]$ at the surface membrane (upper red trace) peaks at $\sim 80 \mu\text{M}$ and later converges to the aggregate $[\text{Ca}^{2+}]$ (~ 20 – $25 \mu\text{M}$). This estimate of submembranous $[\text{Ca}^{2+}]$ was reproducible in multiple cells

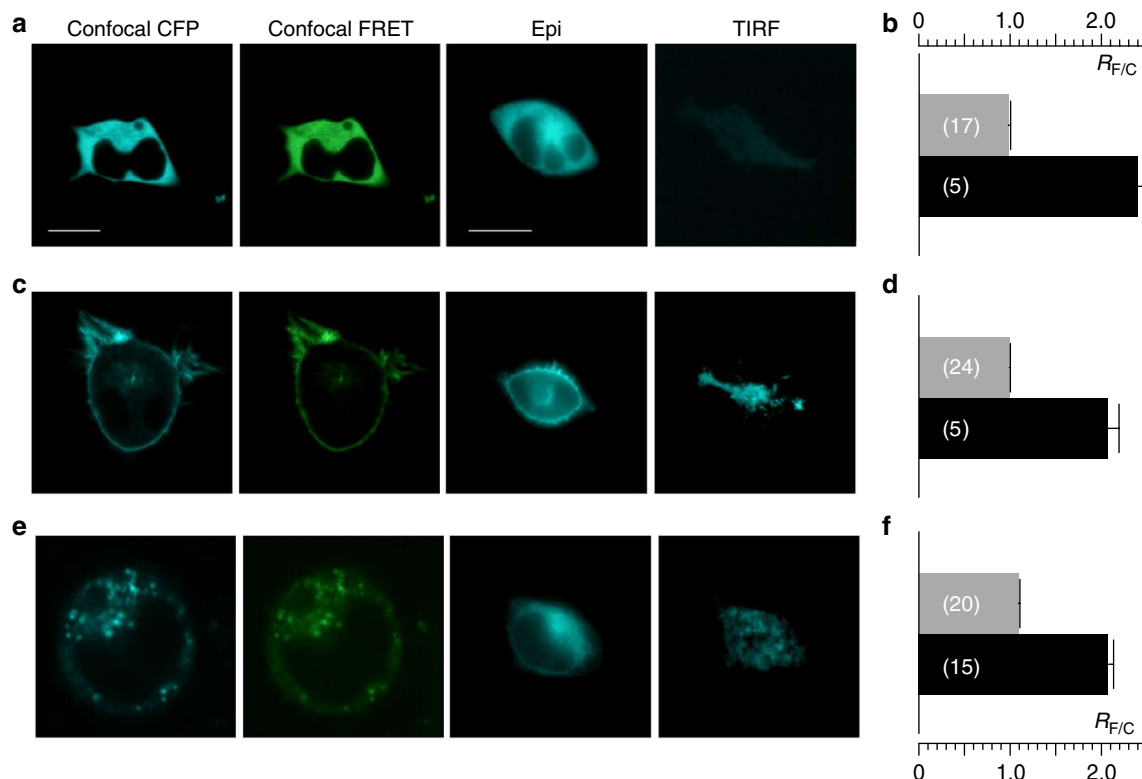


Figure 2 | Ca_v2.2/TN-XL fusion construct preserves function of sensor. (a) Behaviour of free TN-XL. Left to right: confocal (CFP filter), confocal (FRET filter), epi-fluorescence (CFP filter), and TIRF (CFP filter) images of HEK293 cells expressing cytoplasmic TN-XL. White scale bar, 10 μ m. Bar at far left pertains to all confocal images. Bar at middle right pertains to all epifluorescence and TIRF images. (b) TN-XL ratio ($R_{F/C} = S_F/S_C$) measured in resting cells (R_{min}) (grey bar) and in cells under high Ca^{2+} (R_{max}) (black bar). Data shown as mean \pm s.e.m. with number of cells in parentheses. (c,d), Behaviour of TN-XL-Ras (membrane targeted TN-XL). Format as in (a,b), respectively. (e,f), Behaviour of Ca_v2.2/TN-XL (N-type channel fused to TN-XL). Format as in (a,b), respectively.

exhibiting like Ca^{2+} influx, and was thereby taken as the relevant Ca^{2+} input in parallel experiments performed with Ca_v2.2/TN-XL fusion constructs, under TIRF imaging. The green trace in Fig. 4c displays the corresponding sensor output from GECIs in the submembranous TIRF volume, averaged from multiple cells exhibiting Ca^{2+} influx matching that in Fig. 4a. The steady-state plateau of the response (Fig. 4c, grey dashed line at $R_{F/C} = 1.78$), at a near steady Ca^{2+} concentration of ~ 20 – 25μ M, enabled us to calculate $\sim 17.3 \mu$ M as the half-response point of the steady-state response curve for Ca_v2.2/TN-XL constructs in the TIRF volume (Supplementary Methods). This differs from the 2.5μ M half-response point for free TN-XL⁴⁴, consistent with previous observations that sensor performance can change with cellular/molecular environment^{38,42}. Accordingly, steady-state response data for free TN-XL⁴⁴ were shifted along the $[Ca^{2+}]$ axis by $\times 16.3/2.5$ to provide an appropriate steady-state profile for Ca_v2.2/TN-XL constructs (Fig. 4d, green symbols). In all, these steady-state data and the dynamic sensor response (Fig. 4c, green trace) to a specified submembranous Ca^{2+} input (Fig. 4b, upper red trace) furnished the constraints required to deduce a forward transform for Ca_v2.2/TN-XL.

Fig. 4e displays the corresponding state-diagram approximation of Ca_v2.2/TN-XL responsiveness to Ca^{2+} , based on a mechanism for an older troponin-based GECI⁴⁸ (TN-L15). State UB₀ ('unbound') represents the Ca^{2+} -free conformation of the sensor, characterized by a lower FRET-ratio output of R_{min} . On binding of a single Ca^{2+} to the N-lobe of troponin, the sensor adopts one of two alternate 'bound' conformations (B_1 or B_2), both featuring the same elevated FRET-ratio output of R_{mid} . The arrangement, thus far, is identical to that previously established for TN-L15 (ref. 48). The improved performance of TN-XL arises, via engineering the

C-lobe of troponin, to dynamically bind and unbind two signalling Ca^{2+} ions, thereby driving a further conformational change of the sensor⁴⁴. To account for this feature, we allowed two additional Ca^{2+} ions to bind and induce a third bound state^{50,51} (B_3 , dashed box), exhibiting the highest FRET-ratio output of R_{max} . Numerical simulations of this scheme (Supplementary Methods), coupled with error minimization via parameter variation, yielded impressive fits to the target constraints above (Fig. 4c,d, red curves), using the sensor parameter estimates in Table 1. Accordingly, these parameters and the scheme in Fig. 4e furnish a steady-state and dynamic representation of Ca_v2.2/TN-XL responsiveness to Ca^{2+} , a 'forward transform' (Fig. 4f) that is potentially appropriate for making inferences about channel nanodomain Ca^{2+} fluctuations.

Ca_v2.2/TN-XL sensors respond to nanodomain Ca^{2+} signals.

This transform could only be utilized, however, if a substantial fraction of Ca_v2.2/TN-XL sensors respond to channel nanodomain Ca^{2+} signals, as specifically produced by individual channels fluxing Ca^{2+} into their own nanodomain. Thus far, we had only demonstrated that Ca_v2.2/TN-XL sensors in the TIRF volume respond well to a generalized increase in submembranous $[Ca^{2+}]$, but this would occur whether the majority of channel-sensor fusion constructs are properly trafficked to the surface membrane, or still plentiful in submembranous vesicles within the TIRF volume. To address this issue, we again undertook simultaneous recordings of whole-cell Ca^{2+} current and TIRF imaging of Ca_v2.2/TN-XL sensors, but here with high intracellular Ca^{2+} buffering present to restrict Ca^{2+} elevations to the nanodomain of active channels that flux Ca^{2+} . Specifically, we dialysed cells with 10 mM EGTA, yielding a Ca^{2+} nanodomain radius of ~ 40 nm (ref. 13) (Fig. 5, top cartoon),

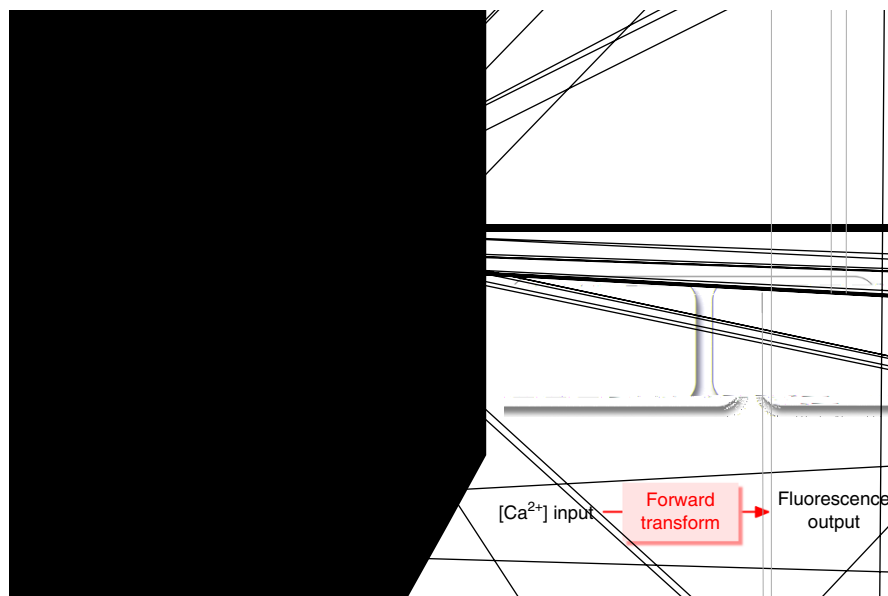


only twofold larger than electron micrographic estimates of Ca^{2+} channel diameters³². Additionally, we only investigated cells with modest Ca^{2+} currents (~ 1 nA with 10 mM Ca^{2+} as charge carrier) and little Ca^{2+} -dependent inactivation²¹ (CDI), so as to exclude Ca^{2+} buffer depletion. Fig. 5a summarizes the results of an exemplar cell satisfying this criterion, with the displayed data evoked by a single voltage pulse. Clearly present is a transient decrease in CFP fluorescence (S_C , cyan trace), accompanied by a corresponding phasic elevation of the FRET ratio $R_{F/C}$ (green trace). Exponential fits (solid black curves) revealed dominant rise and fall times of 880 and 2,000 ms for S_C , and 880 and 400 ms for $R_{F/C}$. Both the return of TN-XL waveforms towards baseline, and the modest CDI of channels under elevated Ca^{2+} buffering²¹ (Fig. 5a compared with Fig. 4a), argue against unintended depletion of Ca^{2+} buffer. Accordingly, these results suggest responsiveness of $\text{Ca}_v2.2/\text{TN-XL}$ sensors to genuine channel nanodomain Ca^{2+} signals. By contrast to

the exemplar, about half the cells with currents of this magnitude and limited CDI exhibited no appreciable change of TN-XL readouts, presumably due to poor trafficking of active channels. Such cells were excluded from further analysis.

Forward transform estimates of nanodomain Ca^{2+} amplitudes.

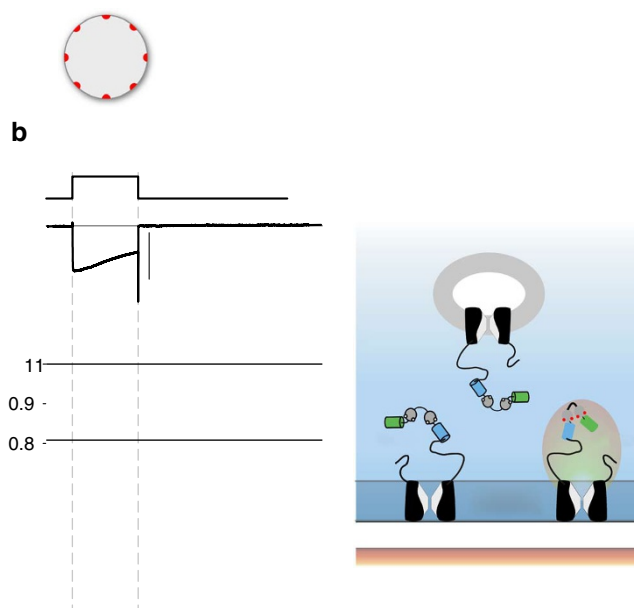
As a prelude to more rigorous assessment of $\text{Ca}_v2.2/\text{TN-XL}$ responses to nanodomain signals, we averaged signals from multiple responsive cells dialysed with 10 mM EGTA. The mean responses (Fig. 5b) were similar to those of the exemplar, with nearly identical characteristic time constants. This reproducibility encouraged us to quantitatively scrutinize these averaged waveforms. In particular, although the robust responses observed here under elevated Ca^{2+} buffering do indicate an appreciable fraction of active channels within the TIRF volume (Fig. 5c, active), the data do not exclude the possibility of a still substantial fraction of channels that



are present in the plasmalemma but fail to open (Fig. 5c, silent), or resident within submembranous vesicles within the TIRF volume (Fig. 5c, intracellular). Such silent and/or intracellular channels would contribute static background fluorescence that could complicate quantitative interpretation. An indication of this scenario comes from exponential extrapolation of the S_C waveform decline (Fig. 5b, dashed curve), which asymptotes in the range of ~ 0.8 . By contrast, under the assumption that all channels are active, simulations of the forward transform in Fig 4e,f indicate that, over a large range of plausible nanodomain Ca^{2+} pulse amplitudes ($\geq 35 \mu\text{M}$),

S_C waveforms would asymptote near Ca^{2+} -saturating levels of ~ 0.5 (Supplementary Fig. S2; Supplementary Methods), as specified by the experimentally determined $1/\alpha_0$ value (defined in Table 1). Hence, the experimentally deduced asymptote of ~ 0.8 (Fig. 5b) suggests that $\sim 40\%$ of $\text{Ca}_V2.2/\text{TN-XL}$ channels are active within the TIRF volume, whereas $\sim 60\%$ of channels are intracellular or silent. Cognizant of this configuration, we correct S_C and $R_{F/C}$ waveforms to reflect only active channels, simply by subtracting $\sim 60\%$ of the baseline amplitude of CFP (S_C) and FRET (S_F) signals, and taking a ratio of these subtracted signals to obtain a corrected $R_{F/C}$. Fig. 6a shows the corrected signals (\bar{S}_C , $\bar{R}_{F/C}$), averaged over multiple cells. These waveforms were then suitable for making inferences about nanodomain Ca^{2+} .

That nanodomain Ca^{2+} signals take the form of equi-amplitude Ca^{2+} pulses, synchronized to the millisecond opening of channels, is widely accepted^{10,12} (cartoon, Fig. 6b); however, the critical amplitude of such pulses (Ca_{spike}) has only been inferred via simulations of Ca^{2+} diffusion^{12–16}. To estimate Ca_{spike} empirically, we analysed the corrected $\text{Ca}_V2.2/\text{TN-XL}$ responses (Fig. 6a), using the forward transform in Fig. 4e,f. The experimental waveforms might initially appear difficult to conceptualize, as each TN-XL sees a different stochastic record of Ca^{2+} pulses driven by single-channel openings. However, because the response of each TN-XL is slow (Table 1; compare Fig. 4b,c), relative to the millisecond duration of individual Ca^{2+} spikes, we can adopt a previously established kinetic simplification¹⁰ that permits the Ca^{2+} -driven forward reaction rates in Fig. 4e to be treated, not as stochastic entities that fluctuate with each Ca^{2+} pulse, but as smoothly changing entities $k_{01} \cdot \text{Ca}_{\text{spike}} \cdot P_O(t)$ and $k_{23} \cdot \text{Ca}_{\text{spike}}^2 \cdot P_O(t)$. Importantly, these entities are to the first order equal for all active $\text{Ca}_V2.2/\text{TN-XL}$ sensors, such that the collective output from multiple sensors, as displayed in Fig. 6a, would approximate that for any individual

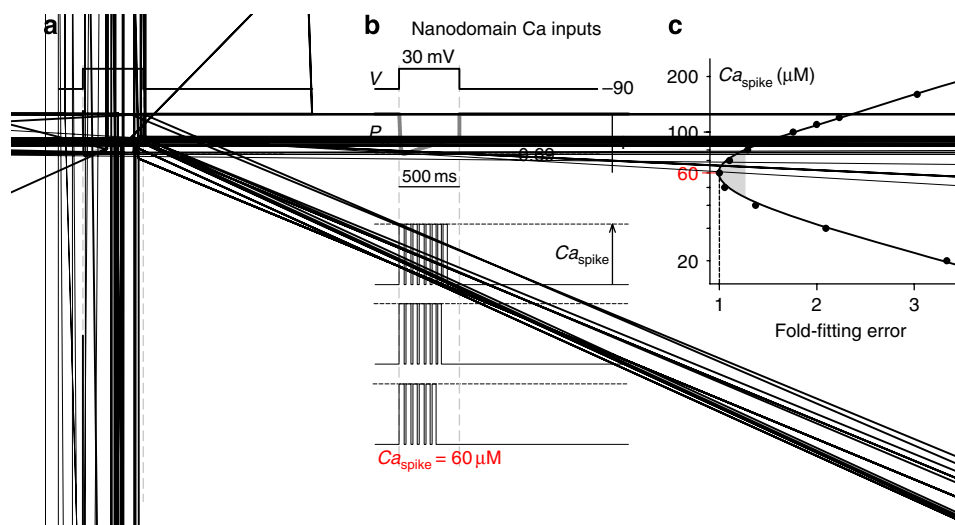


sensor on average. Thus, using our forward transform (Fig. 4e,f) to predict experimental waveforms becomes simple. Single-channel data (Fig. 3e) permit average whole-cell currents (Fig. 5b) to be rescaled as an open probability P_O waveform (Fig. 6a,b); this P_O drives straightforward numerical integration of the differential equations corresponding to the transform in Fig. 4e, and this integration yields predictions of experimental waveforms, with the magnitude of Ca_{spike} , being the only unknown (Supplementary Methods). Whereas presumed Ca_{spike} values of 15 or 240 μM yield predicted $\bar{R}_{F/C}$ trajectories (Fig. 6a, grey smooth curves) that are patently inconsistent with the experimental curve, $Ca_{spike} = 60 \mu M$ produces an impressive fit to data (smooth red curves). Indeed, error analysis (Fig. 6c) confirms 60 μM as a best estimate of Ca_{spike} . As a conservative lower limit, we performed transform analysis on uncorrected waveforms (Fig. 5b), yielding a still-large estimated $Ca_{spike} \sim 15 \mu M$ (Supplementary Fig. S3; Supplementary Methods). Fits to uncorrected data were notably inferior, further prompting us to favour Ca_{spike} estimates from the background-corrected data in Fig. 6a. For these data, the shading in Fig. 6c encompasses fits with errors similar to the minimum, yielding an approximate Ca_{spike} range of 45–80 μM . This estimate, combined with determination of the underlying single-channel current amplitude, can potentially furnish valuable insight into Ca^{2+} diffusion properties within the nanodomain itself (Fig. 7).

Discussion

The fusion of $Ca_v2.2$ channels to the genetically encoded Ca^{2+} sensor TN-XL here furnishes a new tool for detecting submembranous Ca^{2+} signals near these ‘N-type’ Ca^{2+} channels (Fig. 1b). Our particular application concerns the nanodomain Ca^{2+} transients accompanying individual channel openings and closings. These transients have eluded direct experimental comment, until the recent advent of TIRF microscopy to image single-channel activity^{30,31}, and the availability of targetable chemical-fluorescent Ca^{2+} indicators³⁸. Here we demonstrate an alternative approach exploiting TIRF/patch-clamp electrophysiology and our $Ca_v2.2$ /TN-XL fusion. This tactic yields a first empirical estimate of the amplitude of nanodomain Ca^{2+} pulses (Ca_{spike}). This parameter figures crucially in the Ca^{2+} activation of co-localized channels and enzymes², evoked release of nearby neurotransmitter vesicles²⁵, and excitation–transcription coupling^{8,9}.

A limitation of the present study concerns the incomplete targeting of active $Ca_v2.2$ /TN-XL channels to the surface membrane in the TIRF volume, necessitating approximate correction of static background fluorescence. The potential error in such correction renders our Ca_{spike} determination as a coarse approximate estimate. Nonetheless, the approach taken will prove valuable as a means to improve channel trafficking arise, and GECI technology progresses.



With this proviso, we consider other long-sought-after Ca^{2+} channel signalling properties that could, in principle, be accessed with our strategy. First, we estimate the gain factor A , defined as the ratio of Ca_{spike} to unitary current i fluxing through individual Ca^{2+} channels³². As such, the magnitude of A is crucial for local Ca^{2+} channel signalling to downstream nanodomain targets. Given knowledge of Ca_{spike} , we could estimate A itself, so long as the i were known under the conditions of Ca_{spike} determination (Fig. 6, with 10 mM Ca^{2+} as the charge carrier). The single-channel data thus far (Fig. 3c,d) were obtained with 90 mM Ba^{2+} to facilitate resolution of open probability; these data could not be utilized here. The relevant single-channel data for parameter A specification would entail several-fold smaller signals^{25,52}. Nonetheless, despite signals near the limits of detection, we acquired well-resolved unitary currents under these conditions (Fig. 7a). These data yield $i = 0.085 \pm 0.003$ pA ($n = 5$ patches) at 30 mV (as in Fig. 6), resembling values recorded in native $\text{Ca}_v2.2$ channels²⁵. Combining i with our estimates of Ca_{spike} (centre, $\sim 60 \mu\text{M}$; range, $45\text{--}80 \mu\text{M}$), we obtain A , $\sim 700 \mu\text{M/pA}$ (Fig. 7b, shaded regions).

Second, if the distance from the cytoplasmic mouth of the channel to the sensor (r_{sensor}) were also known, near-field Ca^{2+} sensing could comment powerfully on Ca^{2+} diffusion within the nanodomain itself. We therefore gauge r_{sensor} from FRET measured between the CFP of our $\text{Ca}_v2.2/\text{TN-XL}$ fusion, and YFP fused to the base of the channel amino terminus (Fig. 7c). To eliminate crosstalk, YFP within TN-XL itself is replaced with the inert analogue amber⁵³. FRET efficiency was thus determined⁵⁴ (Fig. 7d), yielding an estimated $r_{\text{sensor}} \sim 55 \text{ \AA}$ (Methods).

With both parameter A and r_{sensor} in hand, we scrutinize nanodomain Ca^{2+} diffusion via classic point-source Ca^{2+} diffusion, as given by a generalized Neher-Stern equation^{13,16}

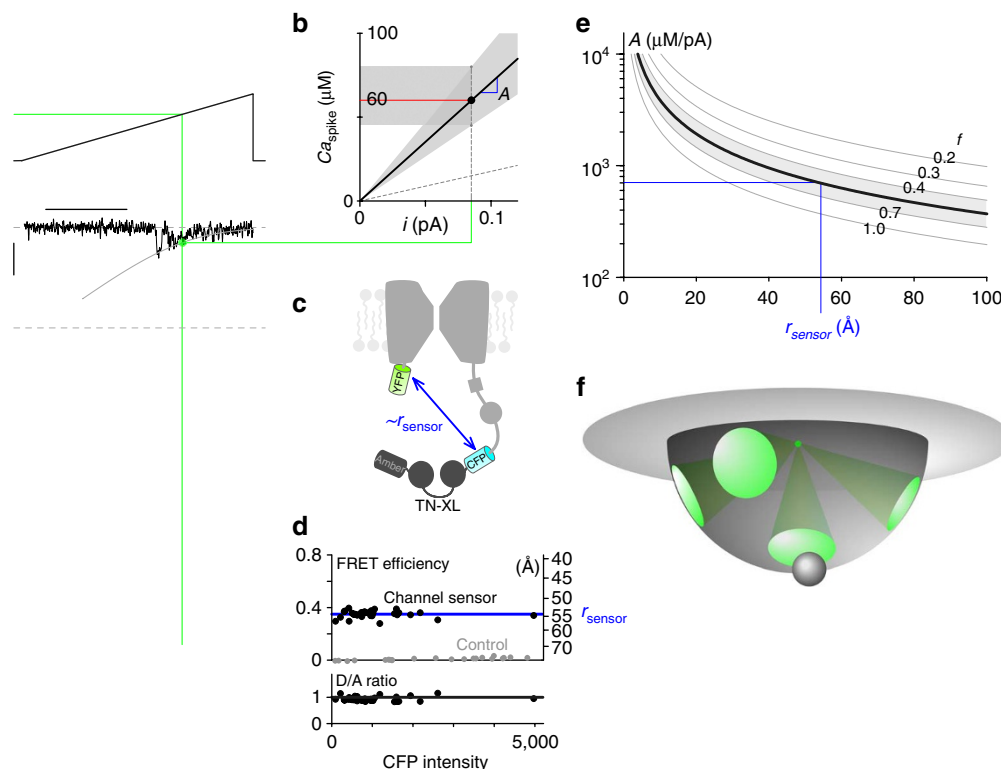
$$A = \frac{\text{Ca}_{\text{spike}}}{i} = \frac{(1/f)}{4 \cdot \pi \cdot F \cdot D_{\text{Ca}} \cdot r_{\text{sensor}}} \cdot \exp \left[\frac{-r_{\text{sensor}}}{\sqrt{D_{\text{Ca}} / (k_{\text{Bon}} \cdot B_{\text{T}})}} \right] \quad (1)$$

where r_{sensor} is the distance of the TN-XL sensor from the point source of Ca^{2+} influx; D_{Ca} is the diffusion coefficient of free Ca^{2+} ; F is Faraday's constant; k_{Bon} is the on rate for Ca^{2+} binding to EGTA; and B_{T} is the internal EGTA concentration (10 mM). The parameter f , specifying the fraction of half-infinite space into which radial Ca^{2+} diffusion occurs, has always been set at unity (Ca^{2+} diffuses into a full half-infinite space), absent any evidence to the contrary. Intriguingly, our estimates of A and r_{sensor} square poorly with the traditional view (Fig. 7e, grey curve with $f=1$), but fit well with $f \sim 0.53$ ($0.53 \times 2\pi$ steradians, solid curve). This outcome may represent an early functional indication of fenestrated Ca^{2+} egress from the channel into cytoplasm (Fig. 7f), according with crystallographic structures of K channels⁵⁵.

Thus, nanodomain Ca^{2+} diffusion could focus Ca^{2+} through particular molecular geometries within the channel-signalling complex, raising the possibility of enhanced preferential signalling to target molecules near or within exit portals (Fig. 7f, grey ball). Indeed, although previous studies elegantly suggest that distinctive unitary current amplitudes i render $\text{Ca}_v2.2$ channels favourable for triggering vesicle fusion²⁵, it is also plausible that differing A and f values also factor into such optimization. The latter possibilities represent an intriguing, but nearly unexplored, realm of Ca^{2+} biology. Although other interpretations are certainly viable, further empirical estimates of Ca_{spike} , parameter A , and r_{sensor} will likely aid in the dawning of this field of inquiry.

Methods

Molecular biology. $\text{Ca}_v2.2/\text{TN-XL}$ ($\text{Ca}_v2.2$ is of human origin (NM000718)) fusion construct was made by PCR, using fusion primers. Pfu polymerase (Stratagene) was used for fidelity. To make $\text{Ca}_v2.2/\text{TN-XL}$, we first generated a $\text{Ca}_v2.2$ channel with the C-terminus truncated at the 2180th amino acid (without a stop codon), yielding $\text{Ca}_v2.2\Delta 2180$ stopless/XbaI in pcDNA3.1. This was made by cutting $\text{Ca}_v2.2$ with Xho I and Xba I, and replacing the resulting fragment with the PCR product amplified from $\text{Ca}_v2.2$ between the Xho I and 2180th amino-acid sites using forward primer 5'-CGCATCAGTTACATGACA TG-3', and reverse primer 5'-CTGTCTAGAAGCACCAGATGTTGACAGCA-3'.



Next, TN-XL was PCR-amplified with an Xba I site upstream of CFP (ATG removed) and a Nhe I/Spe I site downstream of the stop codon of circularly permuted Citrine. The forward and reverse primers used were 5'-CGGCCGCCA CCTCTAGAGTGAGC-3', and 5'-CAGACTAGTGCTAGCTTAGTCCTCGATG TTGTGGC-3' respectively. Finally, the TN-XL PCR fragment was spliced into the $\text{Ca}_v2.2\Delta 2180$ stopless/XbaI construct at the Xba I site to give our $\text{Ca}_v2.2/\text{TN-XL}$ construct.

For the variant construct in Fig. 7c, the circularly permuted Citrine in TN-XL was replaced with circularly permuted amber⁵³, and YFP fused to the amino terminus of $\text{Ca}_v2.2$ after removal of the first 81 amino acids²² (nearly the entire amino terminus). Complete sequence analysis of regions subjected to PCR was performed.

HEK293 cell culture and transfection. HEK293 cells were cultured on No-1 25-mm glass cover slips (Bellco glass) in 10 cm plates. These slips were coated overnight with 0.01% (wt/v; diluted 1:5 in 0.1 M borate buffer) poly-D-lysine (Sigma), and washed with ddH₂O on the day cells were seeded onto the slips. The poly-D-lysine coating facilitates proper whole-cell voltage control at the membrane/glass interface⁵⁶, and also increases electrostatic attraction between the glass surface and cells, thus favouring cell attachment and optimal TIRF imaging. Cells were transiently transfected, using calcium-phosphate precipitation⁵⁴, with $\text{Ca}_v2.2/\text{TN-XL}$, rat brain β_{2a} ⁵⁴, and rat brain $\alpha_{2\delta}$ ⁵⁴ (10 μg each). $\text{Ca}_v2.2$ and β_{2a} -CFP were substituted for $\text{Ca}_v2.2/\text{TN-XL}$ and β_{2a} , respectively, in some experiments. Co-transfection of channels with a number of molecules did not appreciably improve channel trafficking in our system: PI3K and Akt/PKB⁵⁷, ORL receptors⁵⁸, and

dominant-negative dynamin⁵⁹. TN-XL and TN-XL-Ras sensors were transfected using FuGENE6 (Roche).

Electrophysiology. Whole-cell and single-channel current records were obtained at room temperature 1–3 d post-transfection, using patch-clamp amplifiers Axopatch 200B and Axopatch 200A (Axon Instruments), respectively.

For whole-cell recordings, the cells were bathed in external solution containing (in mM): TEA-MeSO₃, 140; HEPES (pH 7.4 with TEA-OH), 10; and CaCl₂, 10; at 300 mOsm, adjusted with glucose. The internal solution contained (in mM): Cs-MeSO₃, 114–135; CsCl, 5; EGTA, 1 or 10; MgCl₂, 1; MgATP, 4; HEPES (pH 7.4 with CsOH), 10; and 295 mOsm with Cs-MeSO₃. In some experiments, 10 μM Fluo 4FF and 2.5 μM Alexa 568 (Invitrogen, Molecular Probes) were included for ratiometric Ca^{2+} determination. Electrodes were pulled from borosilicate glass capillaries (WPI MTW 150-F4) and had pipette resistances ranging from 1.5 to 2.5 MΩ before 75% series resistance compensation. Voltage pulses were applied at 90 s intervals. Currents were filtered at 5 kHz, and digitized at 25 kHz. Leak and capacitance transients subtracted by P/8 protocol. Data acquired and analysed with custom MATLAB scripts (Mathworks, Natick, MA, USA).

Single-channel recordings were all conducted in the on-cell configuration. The bath contained (in mM): K Glutamate, 132; KCl, 5; NaCl, 5; MgCl₂, 3; EGTA, 2; glucose, 10; and HEPES (pH 7.4 adjusted with KOH), 20 at 300 mOsm adjusted with glucose. This bath solution zeroed the membrane potential. The pipette solution contained, (in mM): BaCl₂, 90; TEA-MeSO₃, 20; HEPES (pH 7.4 adjusted with TEA-OH), 10 at 300 mOsm, adjusted with TEA-MeSO₃. In some experiments, 10 mM CaCl₂ was substituted for BaCl₂ and TEA-MeSO₃ correspondingly

increased. To minimize electrical noise, 5–20 M Ω patch pipettes were pulled from ultra-thick-walled (2 mm outer diameter, 1.16 mm inner diameter) borosilicate glass (BF200-116-10, Sutter Instruments), and coated with Sylgard. Seal resistance was ~80 G Ω . Voltage pulses applied at repetition intervals of 5–15 s; data sampled at 70 μ s intervals, and filtered at 2 kHz (Fig. 3c,d) or 700 Hz (Fig. 7a).

TIRF microscopy. On the day of experiments, the cover slips on which cells were cultured were mounted on a custom bath chamber for TIRF imaging. Fluorescence measurements of single cells were performed on a Nikon Eclipse TE2000U microscope, equipped with a Plan Apo 60 \times TIRF objective (NA 1.45 oil immersion). Nikon immersion oil, with $n_d = 1.515$ (23 °C) was used. For TN-XL imaging, CFP excitation was delivered by a 16-mW Melles Griot 561CS 442-nm diode laser. For Fluo 4FF/Alexa 568 imaging, excitation was delivered by a 40-mW Melles Griot IMA100 argon laser featuring a 514-nm line. For TN-XL imaging, the optical path diagrammed in Supplementary Fig. S4 was used, as described below. A high-resolution CoolSNAP HQ CCD camera (Photometrics), driven by IPLab (Scanalytics) scientific imaging software, was used for cell orientation and verification under TIRF microscopy. Fast quantitative data, averaged across single cells, were instead acquired via photomultiplier tubes (PMTs), as follows. Single-cell fluorescent signals was selected by the image-plane pinhole in a D-104C dual-channel photometer (PTI), and sent to a dichroic mirror (510dclp) that divides the fluorescence emission signals into CFP and FRET signals. These two signals passed through their respective emitters (HQ485 per 30 m and HQ545 per 40 m, Chroma), before being captured by two Hamamatsu R1527 PMTs. Fluorescent signals were filtered at 2 kHz and sampled at 25 kHz, and reflect the activity of several thousand Cav2.2/TN-XL molecules. Shutter control, dark-current subtraction, and data acquisition were controlled by custom MATLAB programs. For Fluo 4FF/Alexa 568 imaging, the optical path was modified slightly. Single-cell fluorescence was isolated via the same pinhole and then sent to a dichroic mirror (545 dclp) that parsed signals into Fluo 4FF and Alexa 568 signals. These two signals passed through their respective emitters (545/40 nm bandpass and HQ580 nm lp, Chroma), before being captured by the same PMTs. The apparent K_d for Fluo 4FF/Alexa 568 ratios under our recording conditions was 20 μ M, as determined in live HEK293 cells dialysed with Ca²⁺ dye and a series of calibrated [Ca²⁺] internal solutions.

Widefield FRET microscopy. 3³-FRET efficiency determination, along with estimation of the ratio of donor to acceptor molecules, was performed within individual live HEK293 cells imaged through a image-plane pinhole according to CFP, FRET and YFP filter cubes⁵⁴. Moreover, r_{sensor} in Fig. 7d was estimated using a Forster distance of 49 Å (ref. 54).

Immunoblots. HEK293 cells expressing Cav2.2/TN-XL or TN-XL-Ras, were washed and collected with PBS, centrifuged and resuspended in lysis buffer (20 mM Tris-HCl [pH 7.5], 300 mM sucrose, 1 mM DTT and protease inhibitor cocktail (Roche)). Lysis was completed with freeze-thaw cycles and sonication. Membrane proteins were separated by initial centrifugation (16,000g \times 10 min at 4 °C), followed by solubilizing the resulting pellet in 1% Triton X-100. This solution was then subjected to centrifugation (16,000g \times 10 min at 4 °C), yielding membrane proteins in the supernatant. Membrane proteins were denatured (95 °C \times 1 min) on dilution with TGS buffer (Bio-Rad), and resolved by 5% SDS-PAGE with no CaCl₂ added to the gel. Proteins were transferred to nitrocellulose membranes (Bio-Rad) by cooled transfer (Tris/Glycine transfer buffer/pH 8.3 \times 19 h). After blocking, membranes were sequentially incubated with rabbit polyclonal anti-GFP antibody (Abcam, 1:5,000 dilution, as directed by manufacturer) and HRP-conjugated secondary antibody (Sigma, 1:2400 dilution as recommended by manufacturer). Protein bands were visualized with enhanced chemiluminescence (Pierce ECL, Thermo Scientific).

Data analysis and modelling. Single-channel ramp data were analysed for Cav2.2/TN-XL unitary current and open probability using custom MATLAB programs¹⁰. For the analysis, all patches contained 1 or 2 active channels. TIRF fluorescent signals from Cav2.2/TN-XL were modelled using custom MATLAB scripts, using approaches detailed in Supplementary Methods

Generalization of the Neher-Stern equation (equation (1)), for f values other than unity, was accomplished by considering mass balance and substituting Q_1/f for Q_1 in equation 6 of the original Stern paper¹³.

References

- Berridge, M. J., Lipp, P. & Bootman, M. D. The versatility and universality of calcium signalling. *Nat. Rev. Mol. Cell Biol.* **1**, 11–21 (2000).
- Parekh, A. B. Decoding cytosolic Ca²⁺ oscillations. *Trends Biochem. Sci.* **36**, 78–87 (2011).
- Bautista, D. M. & Lewis, R. S. Modulation of plasma membrane calcium-ATPase activity by local calcium microdomains near CRAC channels in human T cells. *J. Physiol.* **556**, 805–817 (2004).
- Berkefeld, H. et al. BKCa-Cav channel complexes mediate rapid and localized Ca²⁺-activated K⁺ signaling. *Science* **314**, 615–620 (2006).
- Hudmon, A. et al. CaMKII tethers to L-type Ca²⁺ channels, establishing a local and dedicated integrator of Ca²⁺ signals for facilitation. *J. Cell. Biol.* **171**, 537–547 (2005).
- Evans, R. M. & Zamponi, G. W. Presynaptic Ca²⁺ channels--integration centers for neuronal signaling pathways. *Trends Neurosci.* **29**, 617–624 (2006).
- Cheng, H. & Lederer, W. J. Calcium sparks. *Physiol. Rev.* **88**, 1491–1545 (2008).
- Ma, H., Groth, R. D., Wheeler, D. G., Barrett, C. F. & Tsien, R. W. Excitation-transcription coupling in sympathetic neurons and the molecular mechanism of its initiation. *Neurosci. Res.* **70**, 2–8 (2011).
- Dolmetsch, R. Excitation-transcription coupling: signaling by ion channels to the nucleus. *Sci. STKE* **2003**, PE4 (2003).
- Tadross, M. R., Dick, I. E. & Yue, D. T. Mechanism of local and global Ca²⁺ sensing by calmodulin in complex with a Ca²⁺ channel. *Cell* **133**, 1228–1240 (2008).
- Augustine, G. J., Santamaria, F. & Tanaka, K. Local calcium signaling in neurons. *Neuron* **40**, 331–346 (2003).
- Sherman, A., Keizer, J. & Rinzel, J. Domain model for Ca²⁺-inactivation of Ca²⁺ channels at low channel density. *Biophys. J.* **58**, 985–995 (1990).
- Stern, M. D. Buffering of calcium in the vicinity of a channel pore. *Cell Calcium* **13**, 183–192 (1992).
- Simon, S. M. & Llinas, R. R. Compartmentalization of the submembrane calcium activity during calcium influx and its significance in transmitter release. *Biophys. J.* **48**, 485–498 (1985).
- Fogelson, A. L. & Zucker, R. S. Presynaptic calcium diffusion from various arrays of single channels. Implications for transmitter release and synaptic facilitation. *Biophys. J.* **48**, 1003–1017 (1985).
- Naraghi, M. & Neher, E. Linearized buffered Ca²⁺ diffusion in microdomains and its implications for calculation of [Ca²⁺] at the mouth of a calcium channel. *J. Neurosci.* **17**, 6961–6973 (1997).
- Klingauf, J. & Neher, E. Modeling buffered Ca²⁺ diffusion near the membrane: implications for secretion in neuroendocrine cells. *Biophys. J.* **72**, 674–690 (1997).
- Schneggenburger, R. & Neher, E. Intracellular calcium dependence of transmitter release rates at a fast central synapse. *Nature* **406**, 889–893 (2000).
- Sugimori, M., Lang, E. J., Silver, R. B. & Llinas, R. High-resolution measurement of the time course of calcium-concentration microdomains at squid presynaptic terminals. *Biol. Bull.* **187**, 300–303 (1994).
- DeMaria, C. D., Soong, T. W., Alseikhan, B. A., Alvania, R. S. & Yue, D. T. Calmodulin bifurcates the local Ca²⁺ signal that modulates P/Q-type Ca²⁺ channels. *Nature* **411**, 484–489 (2001).
- Liang, H. et al. Unified mechanisms of Ca²⁺ regulation across the Ca²⁺ channel family. *Neuron* **39**, 951–960 (2003).
- Dick, I. E. et al. A modular switch for spatial Ca²⁺ selectivity in the calmodulin regulation of CaV channels. *Nature* **451**, 830–834 (2008).
- Borst, J. G. & Sakmann, B. Calcium current during a single action potential in a large presynaptic terminal of the rat brainstem. *J. Physiol.* **506** (Pt 1), 143–157 (1998).
- Stanley, E. F. Single calcium channels and acetylcholine release at a presynaptic nerve terminal. *Neuron* **11**, 1007–1011 (1993).
- Weber, A. M. et al. N-type Ca²⁺ channels carry the largest current: implications for nanodomains and transmitter release. *Nat. Neurosci.* **13**, 1348–1350 (2011).
- Gryniewicz, G., Poenie, M. & Tsien, R. Y. A new generation of Ca²⁺ indicators with greatly improved fluorescence properties. *J. Biol. Chem.* **260**, 3440–3450 (1985).
- Schermelleh, L., Heintzmann, R. & Leonhardt, H. A guide to super-resolution fluorescence microscopy. *J. Cell. Biol.* **190**, 165–175 (2010).
- Song, L. S., Sham, J. S., Stern, M. D., Lakatta, E. G. & Cheng, H. Direct measurement of SR release flux by tracking 'Ca²⁺ spikes' in rat cardiac myocytes. *J. Physiol. (Lond.)* **512**, 677–691 (1998).
- Axelrod, D., Thompson, N. L. & Burghardt, T. P. Total internal reflection fluorescent microscopy. *J. Microsc.* **129**, 19–28 (1983).
- Demuro, A. & Parker, I. Imaging single-channel calcium microdomains. *Cell Calcium* **40**, 413–422 (2006).
- Navedo, M. F., Amberg, G. C., Nieves, M., Molkentin, J. D. & Santana, L. F. Mechanisms underlying heterogeneous Ca²⁺ sparklet activity in arterial smooth muscle. *J. Gen. Physiol.* **127**, 611–622 (2006).
- Wang, M. C. et al. 3D structure of the skeletal muscle dihydropyridine receptor. *J. Mol. Biol.* **323**, 85–98 (2002).
- Syngne, E. H. A suggested method for extending microscopic resolution into the ultra-microscopic region. *Phil. Mag.* **6**, 356–362 (1928).
- Blinks, J. R., Wier, W. G., Hess, P. & Prendergast, F. G. Measurement of Ca²⁺ concentrations in living cells. *Prog. Biophys. Mol. Biol.* **40**, 1–114 (1982).
- Brini, M. et al. Nuclear Ca²⁺ concentration measured with specifically targeted recombinant aequorin. *Embo J.* **12**, 4813–4819 (1993).
- Montero, M. et al. Monitoring dynamic changes in free Ca²⁺ concentration in the endoplasmic reticulum of intact cells. *Embo J.* **14**, 5467–5475 (1995).
- Rizzuto, R., Simpson, A. W., Brini, M. & Pozzan, T. Rapid changes of mitochondrial Ca²⁺ revealed by specifically targeted recombinant aequorin. *Nature* **358**, 325–327 (1992).
- Tour, O. et al. Calcium Green FIAsh as a genetically targeted small-molecule calcium indicator. *Nat. Chem. Biol.* **3**, 423–431 (2007).

39. Hadley, R. W. & Lederer, W. J. Properties of L-type calcium channel gating current in isolated guinea pig ventricular myocytes. *J. Gen. Physiol.* **98**, 265–285 (1991).
40. Miyawaki, A. *et al.* Fluorescent indicators for Ca^{2+} based on green fluorescent proteins and calmodulin. *Nature* **388**, 882–887 (1997).
41. Tallini, Y. N. *et al.* Imaging cellular signals in the heart *in vivo*: cardiac expression of the high-signal Ca^{2+} indicator GCaMP2. *Proc. Natl Acad. Sci. USA* **103**, 4753–4758 (2006).
42. Heim, N. & Griesbeck, O. Genetically encoded indicators of cellular calcium dynamics based on troponin C and green fluorescent protein. *J. Biol. Chem.* **279**, 14280–14286 (2004).
43. Mori, M. X., Erickson, M. G. & Yue, D. T. Functional stoichiometry and local enrichment of calmodulin interacting with Ca^{2+} channels. *Science* **304**, 432–435 (2004).
44. Mank, M. *et al.* A FRET-based calcium biosensor with fast signal kinetics and high fluorescence change. *Biophys. J.* **90**, 1790–1796 (2006).
45. Colecraft, H. M., Brody, D. L. & Yue, D. T. G-protein inhibition of N- and P/Q-type calcium channels: distinctive elementary mechanisms and their functional impact. *J. Neurosci.* **21**, 1137–1147 (2001).
46. Noceti, F. *et al.* Effective gating charges per channel in voltage-dependent K^{+} and Ca^{2+} channels. *J. Gen. Physiol.* **108**, 143–155 (1996).
47. Jones, L. P., DeMaria, C. D. & Yue, D. T. N-type calcium channel inactivation probed by gating-current analysis. *Biophys. J.* **76**, 2530–2552 (1999).
48. Tay, L. H., Griesbeck, O. & Yue, D. T. Live-cell transforms between Ca^{2+} transients and FRET responses for a troponin-C-based Ca^{2+} sensor. *Biophys. J.* **93**, 4031–4040 (2007).
49. Fang, K. & Colecraft, H. M. Mechanism of auxiliary β -subunit-mediated membrane targeting of L-type ($\text{CaV}1.2$) channels. *J. Physiol.* **589**, 4437–4455 (2011).
50. Linse, S., Helmersson, A. & Forsen, S. Calcium binding to calmodulin and its globular domains. *J. Biol. Chem.* **266**, 8050–8054 (1991).
51. Martin, S. R., Andersson Teleman, A., Bayley, P. M., Drakenberg, T. & Forsen, S. Kinetics of calcium dissociation from calmodulin and its tryptic fragments. A stopped-flow fluorescence study using Quin 2 reveals a two-domain structure. *Eur. J. Biochem.* **151**, 543–550 (1985).
52. Chaudhuri, D., Issa, J. B. & Yue, D. T. Elementary mechanisms producing facilitation of $\text{CaV}2.1$ (P/Q-type) channels. *J. Gen. Physiol.* **129**, 385–401 (2007).
53. Koushik, S. V., Chen, H., Thaler, C., Puhl, H. L. III, & Vogel, S. S. Cerulean, Venus, and VenusY67C FRET reference standards. *Biophys. J.* **91**, L99–L101 (2006).
54. Erickson, M. G., Alseikhan, B. A., Peterson, B. Z. & Yue, D. T. Preassociation of calmodulin with voltage-gated Ca^{2+} channels revealed by FRET in single living cells. *Neuron* **31**, 973–985 (2001).
55. Long, S. B., Campbell, E. B. & Mackinnon, R. Crystal structure of a mammalian voltage-dependent Shaker family K^{+} channel. *Science* **309**, 897–903 (2005).
56. Blunck, R., Starace, D. M., Correa, A. M. & Bezanilla, F. Detecting rearrangements of shaker and NaChBac in real-time with fluorescence spectroscopy in patch-clamped mammalian cells. *Biophys. J.* **86**, 3966–3980 (2004).
57. Viard, P. *et al.* PI3K promotes voltage-dependent calcium channel trafficking to the plasma membrane. *Nat. Neurosci.* **7**, 939–946 (2004).
58. Altier, C. *et al.* ORL1 receptor-mediated internalization of N-type calcium channels. *Nat. Neurosci.* **9**, 31–40 (2006).
59. Green, E. M., Barrett, C. F., Bultynck, G., Shamah, S. M. & Dolmetsch, R. E. The tumor suppressor eIF3e mediates calcium-dependent internalization of the L-type calcium channel $\text{CaV}1.2$. *Neuron* **55**, 615–632 (2007).
60. Kits, K. S., de Vlieger, T. A., Kooi, B. W. & Mansvelder, H. D. Diffusion barriers limit the effect of mobile calcium buffers on exocytosis of large dense cored vesicles. *Biophys. J.* **76**, 1693–1705 (1999).

Acknowledgements

Manu Ben Johny contributed valuable insights to the work. Michael Tadross created acquisition software, as well as advising on numerical simulations and Fluo 4FF imaging. The custom bath chamber for mounting cover slips was a kind gift from Luis Fernando Santana, University of Washington. Supported by a grant from the NIMH (R01 MH65531 to D.T.Y.), and from the NHLBI (Kirschstein-NRSA T32 HL07227-35 to I.E.D.).

Author contributions

L.H.T. established the TIRF/patch-clamp apparatus, designed and performed research, analysed data, and co-wrote the paper. I.E.D. performed extensive electrophysiological experiments, FRET imaging, and data analysis. W.Y. performed western blots and molecular biology. M.M. and O.G. guided use of TN-XL. D.T.Y. conceived experiments and analyses, established and performed numerical simulations, analysed data, made figures, and co-wrote the paper.

Additional information

Supplementary Information accompanies this paper at <http://www.nature.com/naturecommunications>

Competing financial interests: The authors declare no competing financial interests.

Reprints and permission information is available online at <http://npg.nature.com/reprintsandpermissions/>

How to cite this article: Tay, L. H. *et al.* Nanodomain Ca^{2+} of Ca^{2+} channels detected by a tethered genetically encoded Ca^{2+} sensor. *Nat. Commun.* 3:778 doi: 10.1038/ncomms1777 (2012).